# An Inductive and Capacitive Integrated Coupler and Its *LCL* Compensation Circuit Design for Wireless Power Transfer

Fei Lu, *Student Member, IEEE*, Hua Zhang, *Student Member, IEEE*, Heath Hofmann, *Senior Member, IEEE*, and Chunting Chris Mi, *Fellow, IEEE*

***Abstract*—This paper proposes a novel coupler structure for wireless power transfer, which takes advantage of both magnetic and electric fields. The coupler contains four metal structures, two each at the primary and secondary sides, which are capacitively coupled. Each structure consists of long strips of metal sheet to increase its self-inductance, which is then inductively coupled with the other three structures. The structures are vertically arranged and the outer structures are larger than the inner ones to maintain the capacitive couplings. An external *LCL* compensation network is proposed to resonate with the coupler. The resonance provides conduction currents flowing through each plate to establish magnetic fields and displacement currents flowing between different plates corresponding to electric fields. A 100-W output power prototype is designed and implemented to operate at 1.0 MHz, and it achieves 73.6% efficiency from dc source to dc load across an air-gap distance of 18 mm. The contribution of this paper is to propose a concept to transfer power using magnetic and electric fields simultaneously.**

***Index Terms*—Capacitive power transfer (CPT), electric fields, inductive power transfer (IPT), IPT and CPT integrated system, magnetic fields, wireless power transfer (WPT).**

## I. Introduction

INDUCTIVE power transfer (IPT) [1]–[4] and capacitive power transfer (CPT) [5], [6] are two effective methods to transfer power without galvanic contact. The IPT system uses loosely coupled inductive coils to generate magnetic fields [7], [8]. It has been widely applied to the charging of low-power portable devices [9] and high-power electric vehicles [10]. It has the advantage of transferring high power efficiently through a large air-gap distance. The dc–dc efficiency has achieved higher than 95% across 150-mm air-gap distance, which is already comparable with the regular plug-in charger [11], [12].

However, the high-frequency magnetic fields in an IPT system can generate eddy-current losses in the metal nearby, which can result in a significant temperature rise and potential fire hazard [13]. Also, an IPT system usually requires ferrite plates to improve the inductive couplings [14], [15], which can significantly increase the system cost and limit the practical application area of the IPT technology.

Compared to the IPT system, the CPT system has two advantages. First, electric fields used in a CPT system do not generate significant eddy-current losses in nearby metals, and there is no concern about temperature rising. Second, metal plates are used in a CPT system to transfer power [16], which can reduce the system cost and weight. Therefore, the CPT system can be an attractive alternative of the IPT system.

The CPT technology can be used in both short- and long-distance applications. When the transfer distance is within millimeter range, the coupling capacitance can be tens of nanofarad [17], [18], and the transferred power can achieve kilowatt level with over 90% dc–dc efficiency [19], [20]. One benefit of the short-distance CPT system is that the electric fields are mainly confined between the plates and the leakage fields are limited.

From the perspective to extend the application of CPT technology, the long-distance CPT systems are also studied. When the transfer distance increases to 10's or 100's of millimeter, the coupling capacitance is in the range of picofarad. One Challenge in the long-distance CPT system is to transfer higher power using the small capacitance. Therefore, an *LCLC* compensation network is proposed to resonate with the coupling capacitors and provide high output power [21], [22]. There are also two safety concerns in the long-distance CPT system. One is the high voltages and the electric field emission to the surrounding area, and the other is the parasitic displacement current to the nearby metal. Although the eddy-current losses are eliminated, the interaction between the CPT system and the metal foreign object should also be studied in future research.

Considering the limitations of long-distance CPT system, one effective method to promote its application is to combine it with the more developed IPT technology [23], [24]. The IPT system

Manuscript received September 23, 2016; revised December 25, 2016 and February 25, 2017; accepted April 11, 2017. Date of publication April 25, 2017; date of current version September 18, 2017. Paper 2016-TSC-1014.R2, presented at the 2016 IEEE Energy Conversion Congress and Exposition, Milwaukee, WI, USA, Sep. 18–22, and approved for publication in the IEEE Transactions on Industry Applications by the Transportation Systems Committee of the IEEE Industry Applications Society. *(Corresponding author: Chunting Chris Mi.)*

F. Lu is with the University of Michigan–Ann Arbor, Ann Arbor, MI 48109, USA, and also with San Diego State University, San Diego, CA 92182, USA (e-mail: feilu@umich.edu).

H. Zhang is with San Diego State University, San Diego, CA 92182, USA, and also with Northwestern Polytechnical University, Xi'an 710072, China (e-mail: hzhang@mail.sdsu.edu).

H. Hofmann is with the University of Michigan–Ann Arbor, Ann Arbor, MI 48109, USA (e-mail: hofmann@umich.edu).

C. C. Mi is with San Diego State University, San Diego, CA 92182, USA (e-mail: mi@ieee.org).

Color versions of one or more of the figures in this paper are available online at http://ieeexplore.ieee.org.

Digital Object Identifier 10.1109/TIA.2017.2697838

usually requires external capacitors to resonate with the coils, and the CPT system usually needs external inductors to establish resonance. Therefore, the couplers in IPT and CPT systems can be combined together, which results in an IPT–CPT combined system [23]. Furthermore, The inductive and capacitive couplers can be integrated into a single coupler [24], which means the "coils" of the IPT system can also act as the "plates" of the CPT system and vice versa. Considering the *LCC* network used in an IPT system [25] and the *LCLC* network used in a CPT system [21], an *LCL* compensation network can be used to resonate with the integrated coupler. Compared to [24], this paper provides more detailed circuit analysis and simulation results. Compared to the previous combined system described in [23], this paper has three differences.

First, there is only one coupler in this system, whereas there are two couplers in [23]. The integrated coupler in this paper can generate magnetic and electric fields simultaneously. The two couplers in [23] generate the two fields separately. Second, the circuit model of the coupler is different. There are both inductive and capacitive couplings in the integrated coupler, which make its circuit model complicated. Whereas, the circuit models of the two couplers in [23] are relatively simpler. Third, the compensation circuit topology is different. In this design, since the self-inductance of the integrated coupler is limited, an *LCL* compensation circuit is required. In [23], the coil inductance is large enough, so only an *LC* circuit is used. In future research, the compensation circuit can be eliminated to further simplify the system structure.

## II. Inductive and Capacitive Integrated Coupler Design

### A. Coupler Structure

The integrated coupler should realize both inductive and capacitive couplings. In a four-plate capacitive coupler [6], the size of the plates is different to realize capacitive couplings. Furthermore, to increase the inductances of the plates and acquire inductive couplings between them, the plates can be cut to long strips. Therefore, there are in total four strips in this coupler: $P_1$, $P_2$, $P_3$, and $P_4$. Strips $P_1$ and $P_2$ are placed at the primary side as a power transmitter, and $P_3$ and $P_4$ are placed at the secondary side as a power receiver. The structure of this inductive and capacitive integrated coupler is shown in Fig. 1.

Fig. 1(a) shows the detail of the primary-side strips $P_1$ and $P_2$. In this design, the coupler is symmetric from the primary to secondary side, so $P_3$ and $P_4$ have the same structure as $P_1$ and $P_2$. Each strip is folded with aluminum sheets to increase the self-inductance. Strip $P_1$ is larger than strip $P_2$ to realize the capacitive coupling with the secondary-side strips. There are two kinds of currents flowing in this integrated coupler; conductive currents and displacement currents. The conductive currents generate magnetic fields, which contribute to the inductive coupling. The displacement currents between the strips relate to the capacitive couplings.

Fig. 1(b) shows the three-dimensional (3-D) view of the integrated coupler structure. Polyimide tape is used to provide insulation between adjacent strips. Nylon spacers are used to separate the primary and secondary strips and provide the air-gap distance.

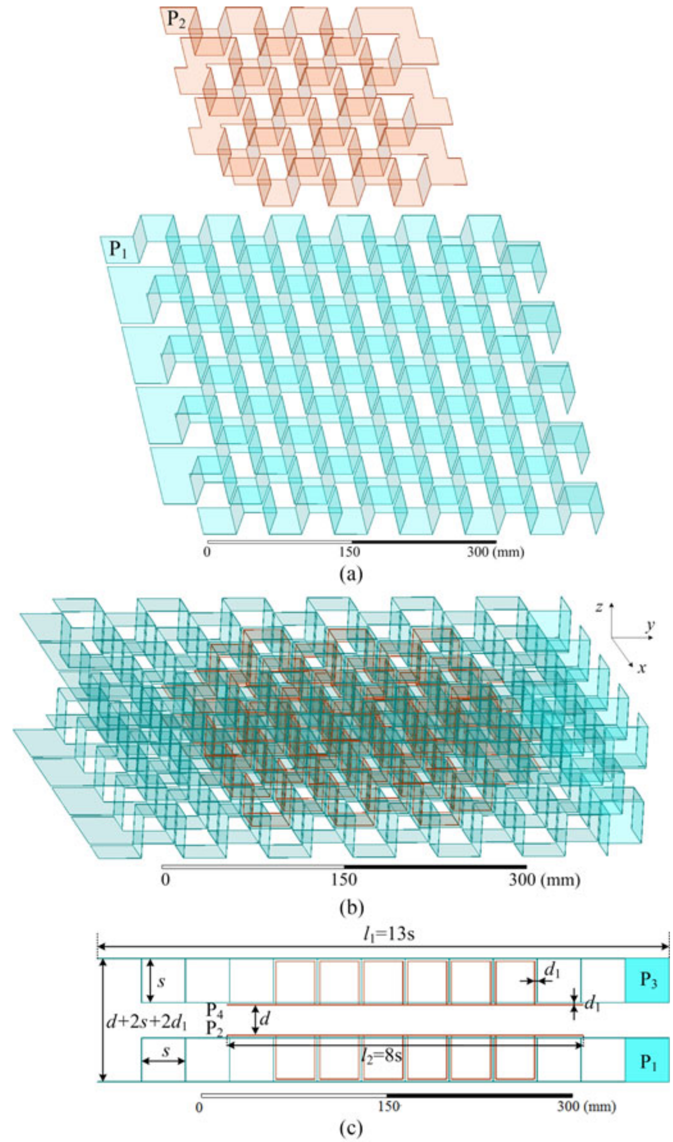


Fig. 1. Structure of the inductive and capacitive integrated coupler. (a) Primary-side detail, (b) 3-D view, and (c) front view.

Fig. 1(c) shows the front view and dimensions of the integrated coupler. Strips $P_3$ and $P_4$ are on the top of $P_1$ and $P_2$. The aluminum sheet, with a thickness $t_{\mathrm{Al}} = 0.2$ mm, is folded to a square shape, and the size of each square is defined as $s$. Due to the aluminum sheet available in the lab, the total length of $P_1$ and $P_3$ is predetermined to be $l_1 = 13s$, and the total length of $P_2$ and $P_4$ is $l_2 = 8s$ to simplify the design process. The distance between $P_1$ and $P_2$ is equal to the distance between $P_3$ and $P_4$, which is defined as $d_1$. Distance $d_1$ can be adjusted by the thickness of the insulation tape. The air-gap distance between the primary and secondary side is defined as $d$. In this specific design, considering the size of the aluminum sheet available in the lab, $s$ is set to be 36 mm. Therefore, $d$ and $d_1$ are the two remaining parameters need to be determined in the following design.

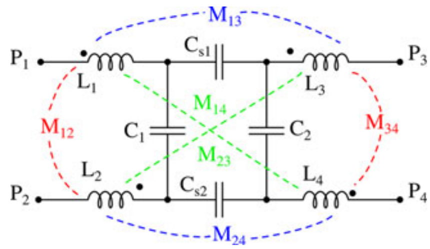


Fig. 2. Equivalent circuit model of the coupler.

### B. Circuit Model

The circuit model of the designed integrated coupler is shown in Fig. 2. The self-inductances of the four strips are defined as $L_1$, $L_2$, $L_3$, and $L_4$. There are inductive couplings between each pair of the strips, resulting in six mutual inductances: $M_{12}$, $M_{13}$, $M_{14}$, $M_{23}$, $M_{24}$, and $M_{34}$. The polarity of the inductive couplings is also identified in Fig. 2, which will be used in the following circuit analysis. The circuit analysis in Section III will show that the mutual inductance $M_{13}$, $M_{14}$, $M_{23}$, and $M_{24}$ contribute to transferring power from the primary to secondary side, and the equivalent mutual inductance $M_{\rm eq}$ is defined as

$$M_{\rm eq} = M_{13} + M_{14} + M_{23} + M_{24}. \tag{1}$$

There are also capacitive couplings between the strips. According to Zhang *et al.* [6], there are six coupling capacitances in the coupler. Since the cross-coupling capacitances between $P_1$ and $P_4$, and between $P_2$ and $P_3$, are relatively small, they are neglected in this design to simplify the circuit model. The capacitance between $P_1$ and $P_2$ is defined as $C_1$, and the capacitance between $P_3$ and $P_4$ is defined as $C_2$. Because of the symmetry of the coupler, there exists $C_1 = C_2$. The coupling between $P_1$ and $P_3$ is defined as $C_{\rm s1}$, and the coupling between $P_2$ and $P_4$ is defined as $C_{\rm s2}$. In Fig. 2, $C_{\rm s1}$ and $C_{\rm s2}$ are in series, which results in an equivalent capacitor $C_{\rm s} = C_{\rm s1}C_{\rm s2}/(C_{\rm s1}+C_{\rm s2})$. $C_1$ and $C_2$ can be defined as the self-capacitances of the coupler, and $C_{\rm s}$ can be defined as the mutual capacitance.

### C. Maxwell Simulation

The finite element analysis (FEA) by Maxwell is used to simulate the plate parameters in different dimensions. It can perform both magnetic and electric field simulations, which provide the inductances and capacitances of the coupler, respectively. When the air-gap distance $d$ varies from 10 to 25 mm, and the plate distance $d_1$ varies from 0.5 to 4.0 mm, the Maxwell-simulated parameters are shown in Fig. 3.

In the electric fields simulation, Fig. 3(a) shows that the self-capacitance $C_1$ decreases with the increasing plate distance $d_1$, and the air-gap $d$ does not affect $C_1$. Fig. 3(b) shows that the mutual capacitance $C_{\rm s}$ decreases with the increasing air-gap $d$, and the plate distance $d_1$ does not affect $C_{\rm s}$. In the magnetic fields simulation, Fig. 3(c) shows that equivalent mutual inductance $M_{\rm eq}$ also decreases with the increasing air-gap distance $d$, and the plate distance $d_1$ does not affect $M_{\rm eq}$.

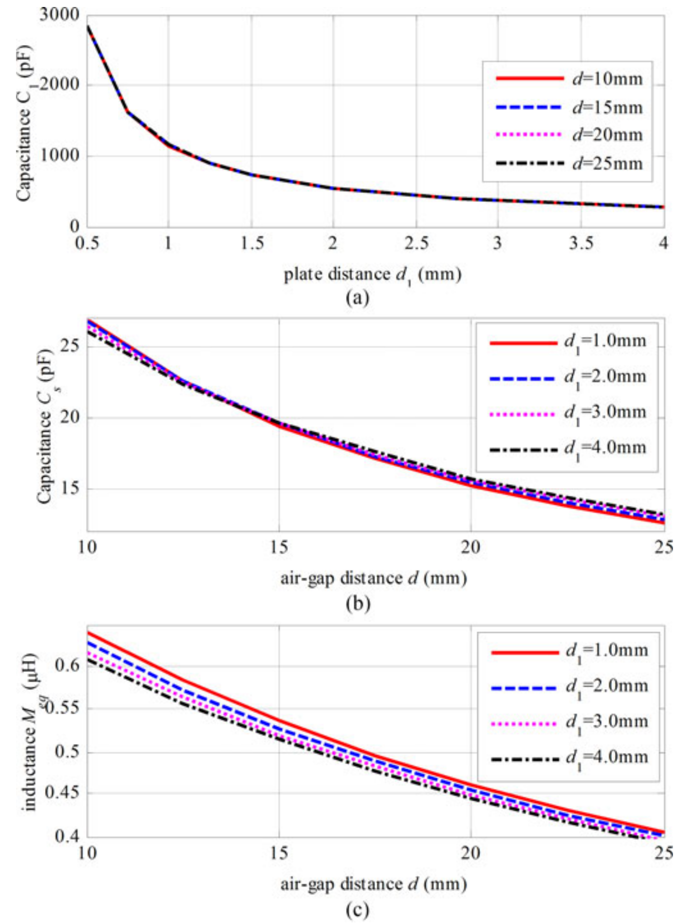


Fig. 3. Maxwell-simulated parameters when $d$ and $d_1$ vary. (a) Capacitance $C_1$, (b) capacitance $C_{\rm s}$, and (c) inductance $M_{\rm eq}$.

Considering the simulation results in Fig. 3(a) and the thickness of the polyimide tape available in the lab, the plate distance $d_1$ is set to 1.2 mm, and the resulting capacitance $C_1$ is 910 pF. Compared to the self-capacitances in previous references [21]–[23], this $C_1$ is relatively large to reduce the required resonant inductance. Then, considering the simulation results in Fig. 3(b) and (c) and the nylon spacer size available in the lab, the air-gap distance is set to 18 mm. The resulting mutual capacitance $C_{\rm s}$ is 16.7 pF and the equivalent mutual inductance $M_{\rm eq}$ is 0.49 $\mu$H. Based on the available materials in the lab, the dimensions of the coupler are shown in Table I, and the corresponding circuit parameters are simulated in Maxwell and also presented.

## III. *LCL* Compensation Circuit Topology for the Integrated Coupler

### A. Circuit Topology

Based on the *LCC* compensation circuit for an IPT system and the *LCLC* compensation for a CPT system, a double-sided *LCL* compensation circuit topology is proposed to resonate with the integrated coupler, which is shown in Fig. 4. There are both magnetic and electric fields generated by the integrated coupler to transfer power.

TABLE I
DIMENSIONS AND MAXWELL-SIMULATED CIRCUIT PARAMETERS OF THE INTEGRATED COUPLER

| Parameter | Design Value | Parameter | Design Value |
|---|---|---|---|
| $l_1$ | 468 mm | $l_2$ | 288 mm |
| $d$ | 18 mm | $d_1$ | 1.2 mm |
| $s$ | 36 mm | $t_{A1}$ | 0.2 mm |
| $L_1$ ($L_3$) | 2.06 $\mu$H | $L_2$ ($L_4$) | 0.76 $\mu$H |
| $M_{12}$ ($M_{34}$) | 0.55 $\mu$H | $M_{14}$ ($M_{23}$) | 0.08 $\mu$H |
| $M_{13}$ | 0.19 $\mu$H | $M_{24}$ | 0.15 $\mu$H |
| $C_1$ ($C_2$) | 910 pF | $C_{s1}$ ($C_{s2}$) | 33.4 pF |
| $M_{eq}$ | 0.49 $\mu$H | $C_s$ | 16.7 pF |

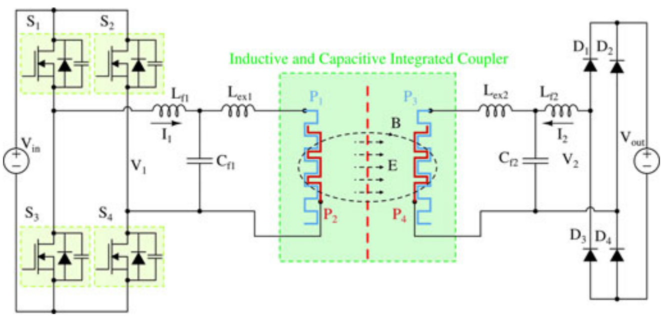


Fig. 4. Circuit topology of a double-sided *LCL* compensated system with an integrated coupler.

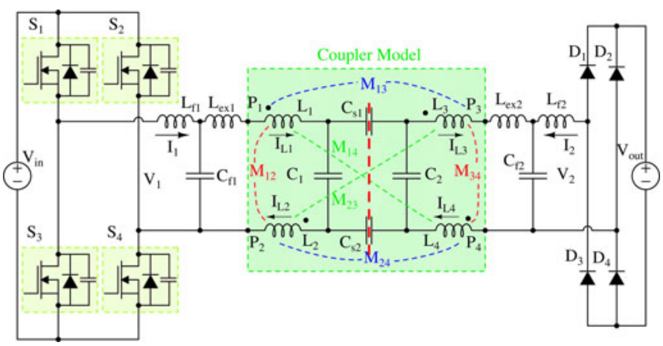


Fig. 5. Equivalent circuit of the inductive and capacitive integrated system.

Since the Maxwell simulations in Table I show that the self-inductances of the coupler are very small, two large external inductors $L_{ex1}$ and $L_{ex2}$ are required to connect in series with the coupler to increase the equivalent inductances. This can also help to reduce the switching frequency of the system. Two pairs of resonances $L_{f1}$–$C_{f1}$ and $L_{f2}$–$C_{f2}$ are used at the input and output side to convert the voltage sources to current ones. They also act as low-pass filters to reduce the harmonics current injected to the resonant circuit.

A full-bridge inverter with four MOSFETs is used at the transmitter side to generate ac excitation to the resonant tank. An uncontrolled diode rectifier is used at the receiver side to provide dc current to serve the battery load. Therefore, the voltages $V_1$ and $V_2$ are both in square waves.

When the integrated coupler is represented by its circuit model, the equivalent circuit of the system is shown in Fig. 5. The polarity of the connection to the integrated coupler should be paid attention to make sure that the contributions of the inductive and capacitive couplings are in the same direction to maximize the output power. The detailed circuit analysis will be presented later.

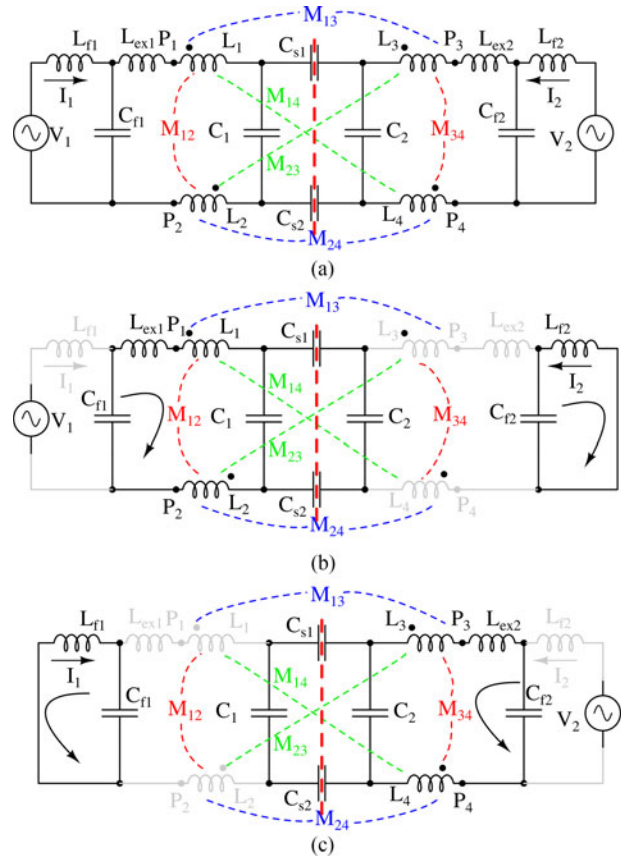


Fig. 6. FHA of the inductive and capacitive integrated system. (a) Simplified circuit topology, (b) excited only by input source, and (c) excited only by output source.

## *B. Circuit Working Principle*

The fundamental harmonics approximation (FHA) method is used to analyze the working principle of the resonant circuit, as shown in Fig. 6. The square wave input and output are replaced by two sinusoidal voltages, and the high-order harmonics components are neglected, which results in a simplified circuit topology in Fig. 6(a). The power losses in the circuit components are also neglected to simplify the circuit. Furthermore, the superposition theorem is further used to analyze the input and output voltages separately.

Fig. 6(b) shows the system excited only by the input source, where two parallel resonances in the circuit are highlighted, and the resonant frequency is defined as $\omega_0$. In this way, there is no current flowing through $L_{f1}$ and $L_{ex2}$, and the circuit analysis process can be significantly simplified. The inductor $L_{f2}$ and capacitor $C_{f2}$ form the first resonance, which is expressed as

$$L_{f2}C_{f2} = \frac{1}{\omega_0^2}. \tag{2}$$

The external inductor $L_{\mathrm{ex}1}$, the coupler inductances $L_1$, $L_2$, and mutual inductance $M_{12}$ are considered together as an equivalent primary inductance $L_{\mathrm{eq}1}$, which is expressed as

$$L_{\mathrm{eq}1} = L_{\mathrm{ex}1} + L_1 + L_2 + 2M_{12}. \tag{3}$$

In the circuit model of the integrated coupler, the capacitors $C_1$, $C_2$, $C_{\mathrm{s}1}$, and $C_{\mathrm{s}2}$ form an equivalent capacitance to the primary side, which can be expressed as

$$C_{\mathrm{eq}1} = C_1 + \frac{C_s C_2}{C_s + C_2} = \frac{C_1 C_2 + C_s C_1 + C_s C_2}{C_s + C_2}. \tag{4}$$

The primary equivalent inductance $L_{\mathrm{eq}1}$, the equivalent capacitance $C_{\mathrm{eq}1}$, and the capacitance $C_{\mathrm{f}1}$ form the second resonance in Fig. 6(b), which is expressed as

$$\omega_0 L_{\mathrm{eq}1} - \frac{1}{\omega_0 C_{\mathrm{eq}1}} - \frac{1}{\omega_0 C_{f1}} = 0. \tag{5}$$

In Fig. 6(b), the voltage on $C_2$ is caused by the capacitive coupling, which is expressed as

$$V_{C2} = V_1 \cdot \left(-\frac{C_{f1}}{C_{eq1}}\right) \cdot \frac{C_s}{C_s + C_2}. \tag{6}$$

By substituting (4) into (6), the $C_2$ voltage is simplified as

$$V_{C2} = -V_1 \cdot \frac{C_s C_{f1}}{C_1 C_2 + C_s C_1 + C_s C_2}. \tag{7}$$

In Fig. 6(b), the voltage on $L_3$ is caused by the inductive couplings, and expressed by the mutual inductance $M_{13}$ and $M_{23}$. Considering the polarity of the connection of $L_3$, the voltage on $L_3$ is expressed as

$$V_{L3} = j\omega_0 M_{13} I_{L1} + j\omega_0 M_{23} I_{L2}. \tag{8}$$

The current $I_{\mathrm{L}1}$ and $I_{\mathrm{L}2}$ are expressed as

$$I_{L1} = I_{L2} = -V_1 \cdot j\omega_0 C_{f1}. \tag{9}$$

Therefore, the voltage $V_{\mathrm{L}3}$ is simplified to be

$$V_{L3} = V_1 \cdot (M_{13} + M_{23}) \cdot \omega_0^2 C_{f1}. \tag{10}$$

The voltage on $L_4$ is caused by the mutual inductances $M_{14}$ and $M_{24}$, and it can be expressed as

$$V_{L4} = j\omega_0 M_{14} I_{L1} + j\omega_0 M_{24} I_{L2}. \tag{11}$$

It is further simplified as

$$V_{L4} = V_1 \cdot (M_{14} + M_{24}) \cdot \omega_0^2 C_{f1}. \tag{12}$$

Then, the voltage across $C_{\mathrm{f}2}$ is expressed as

$$\begin{aligned} V_{Cf2} &= -V_{L3} - V_{L4} + V_{C2} \\ &= -V_1 \cdot (M_{13} + M_{14} + M_{23} + M_{24}) \cdot \omega_0^2 C_{f1} \\ &\quad - \frac{V_1 \cdot C_s C_{f1}}{C_1 C_2 + C_s C_1 + C_s C_2}. \end{aligned} \tag{13}$$

Therefore, the output current $(-I_2)$ to the load is given as

$$\begin{aligned} -I_2 &= -V_{Cf2} \cdot j\omega_0 C_{f2} \\ &= V_1 \cdot \frac{(M_{13} + M_{14} + M_{23} + M_{24}) \cdot j\omega_0 C_{f1}}{L_{f2}} \\ &\quad + \frac{V_1 \cdot j\omega_0 C_s C_{f1} C_{f2}}{C_1 C_2 + C_s C_1 + C_s C_2}. \end{aligned} \tag{14}$$

Fig. 6(c) shows the system excited only by the output source, and there are also two parallel resonances highlighted, which will be analyzed using similar process in Fig. 6(b). The inductor $L_{\mathrm{f}1}$ and capacitor $C_{\mathrm{f}1}$ form one resonance, which is expressed as

$$L_{f1} C_{f1} = \frac{1}{\omega_0^2}. \tag{15}$$

The equivalent secondary inductance $L_{\mathrm{eq}2}$ and capacitance $C_{\mathrm{eq}2}$ are defined as

$$\begin{cases} L_{\mathrm{eq}2} = L_{\mathrm{ex}2} + L_3 + L_4 + 2M_{34} \\ C_{\mathrm{eq}2} = C_2 + \frac{C_s C_1}{C_s + C_1} = \frac{C_1 C_2 + C_s C_1 + C_s C_2}{C_s + C_1} \end{cases}. \tag{16}$$

The other resonance forming by the inductance $L_{\mathrm{eq}2}$, the capacitances $C_{\mathrm{eq}2}$ and $C_{\mathrm{f}2}$ is expressed as

$$\omega_0 L_{\mathrm{eq}2} - \frac{1}{\omega_0 C_{\mathrm{eq}2}} - \frac{1}{\omega_0 C_{f2}} = 0. \tag{17}$$

In Fig. 6(c), the voltage across $C_1$ is caused by capacitive coupling, and expressed as

$$V_{C1} = V_2 \cdot \left(-\frac{C_{f2}}{C_{eq2}}\right) \cdot \frac{C_s}{C_s + C_1}. \tag{18}$$

By submitting (16) into (18), the $C_1$ voltage is simplified as

$$V_{C1} = -V_2 \cdot \frac{C_s C_{f2}}{C_1 C_2 + C_s C_1 + C_s C_2}. \tag{19}$$

The voltages $V_{\mathrm{L}1}$ and $V_{\mathrm{L}2}$ across $L_1$ and $L_2$ are caused by the inductive couplings, and relate to the mutual inductances $M_{13}$, $M_{14}$, $M_{23}$, and $M_{24}$. Similarly, the voltages are expressed as

$$\begin{cases} V_{L1} = -V_2 \cdot (M_{13} + M_{14}) \cdot \omega_0^2 C_{f2} \\ V_{L2} = -V_2 \cdot (M_{23} + M_{24}) \cdot \omega_0^2 C_{f2} \end{cases}. \tag{20}$$

Then, the voltage across $C_{\mathrm{f}1}$ is expressed as

$$\begin{aligned} V_{Cf1} &= V_{L1} + V_{L2} + V_{C1} \\ &= -V_2 \cdot (M_{13} + M_{14} + M_{23} + M_{24}) \cdot \omega_0^2 C_{f2} \\ &\quad - \frac{V_2 \cdot C_s C_{f2}}{C_1 C_2 + C_s C_1 + C_s C_2}. \end{aligned} \tag{21}$$

Therefore, the input voltage $I_1$ is expressed as

$$\begin{aligned} I_1 &= V_{Cf1} \cdot j\omega_0 C_{f1} \\ &= -V_2 \cdot \frac{(M_{13} + M_{14} + M_{23} + M_{24}) j\omega_0 C_{f2}}{L_{f1}} \\ &\quad - \frac{V_2 \cdot j\omega_0 C_s C_{f1} C_{f2}}{C_1 C_2 + C_s C_1 + C_s C_2}. \end{aligned} \tag{22}$$

Considering (2) and (15), the input and output current are further simplified as

$$\begin{cases} I_1 = -V_2 \cdot \frac{j(M_{13}+M_{14}+M_{23}+M_{24})}{\omega_0 L_{f1} L_{f2}} - \frac{V_2 \cdot j\omega_0 C_s C_{f1} C_{f2}}{C_1 C_2 + C_s C_1 + C_s C_2} \\ -I_2 = V_1 \cdot \frac{j(M_{13}+M_{14}+M_{23}+M_{24})}{\omega_0 L_{f1} L_{f2}} + \frac{V_1 \cdot j\omega_0 C_s C_{f1} C_{f2}}{C_1 C_2 + C_s C_1 + C_s C_2} \end{cases}. \tag{23}$$

Since an uncontrolled diode rectifier is used at the secondary side, the output voltage $V_2$ is in phase with the output current $(-I_2)$. The first equation in (23) shows that $I_1$ is 90° lagging $V_2$, and the second equation shows that $V_1$ is also lagging $(-I_2)$ by 90°. Therefore, the input voltage $V_1$ is also in phase with the input current $I_1$. According to (23), the system power is calculated as

$$P_{out} = \left[ \frac{M_{13}+M_{14}+M_{23}+M_{24}}{\omega_0 L_{f1} L_{f2}} + \frac{\omega_0 C_s C_{f1} C_{f2}}{C_1 C_2 + C_s C_1 + C_s C_2} \right] \cdot |V_1| \cdot |V_2|. \tag{24}$$

From (23), it can also be shown that $P_{\text{in}} = P_{\text{out}}$, which is consistent with the assumption to neglect circuit components losses and also validates the previous circuit analysis. The power contributions by inductive and capacitive couplings are defined as $P_{\text{IPT}}$ and $P_{\text{CPT}}$, which are expressed as

$$\begin{cases} P_{\text{IPT}} = \frac{M_{13}+M_{14}+M_{23}+M_{24}}{\omega_0 L_{f1} L_{f2}} \cdot |V_1| \cdot |V_2| \\ P_{\text{CPT}} = \frac{\omega_0 C_s C_{f1} C_{f2}}{C_1 C_2 + C_s C_1 + C_s C_2} \cdot |V_1| \cdot |V_2| \end{cases}. \tag{25}$$

The polarity of the connection in the integrated coupler determines the sign of the mutual inductance $M_{13}$, $M_{14}$, $M_{23}$, and $M_{24}$. When the inductive power $P_{\text{IPT}}$ and capacitive power $P_{\text{CPT}}$ are both positive, the system power is maximized.

## IV. Design Example With the Integrated Coupler

### A. Power Ratio Calculation

According to (25), the power ratio between the IPT and CPT couplings is defined to be $r_{\text{I--C}}$, and expressed as

$$r_{I-C} = \frac{\omega_0^2 \cdot (M_{13}+M_{14}+M_{23}+M_{24}) \cdot (C_1 C_2 + C_s C_1 + C_s C_2)}{C_s}. \tag{26}$$

If the equivalent inductive coupling coefficient $k_{\text{I}}$ and the capacitive coupling coefficient $k_{\text{C}}$ [6] are defined as

$$\begin{cases} k_I = \frac{M_{13}+M_{14}+M_{23}+M_{24}}{\sqrt{L_{eq1} L_{eq2}}} \\ k_C = \frac{C_s}{\sqrt{(C_1+C_s)\cdot(C_2+C_s)}} \end{cases}. \tag{27}$$

Considering (4), (16), and (7), the power ratio is expressed as

$$r_{I-C} = \frac{k_I}{k_C} \cdot \omega_0^2 \cdot \sqrt{L_{\text{eq}1} L_{\text{eq}2} C_{\text{eq}1} C_{\text{eq}2}}. \tag{28}$$

TABLE II
System Specifications and Circuit Parameters

| Parameter | Design Value | Parameter | Design Value |
|---|---|---|---|
| $V_{\text{in}}$ | 50 V | $V_{\text{out}}$ | 50 V |
| $f_{\text{sw}}$ | 1 MHz | $C_{\text{s}}$ | 16.7 pF |
| $L_{\text{f}1}$ ($L_{\text{f}2}$) | 1.54 $\mu$H | $C_{\text{f}1}$ ($C_{\text{f}2}$) | 16.5 nF |
| $L_1$ ($L_3$) | 2.06 $\mu$H | $C_1$ ($C_2$) | 910 pF |
| $L_2$ ($L_4$) | 0.76 $\mu$H | $M_{\text{eq}}$ | 0.49 $\mu$H |
| $L_{\text{ex1}}$ | 24.8 $\mu$H | $L_{\text{ex2}}$ | 25.3 $\mu$H |
| $k_{\text{I}}$ | 1.8% | $k_{\text{C}}$ | 1.8% |

Considering (5) and (17), if $C_{\text{f}1} >> C_{\text{eq}1}$ and $C_{\text{f}2} >> C_{\text{eq}2}$, the power ratio is approximated as

$$r_{I-C} \approx \frac{k_I}{k_C}. \tag{29}$$

It means the power ratio is approximately the ratio between the inductive and capacitive coupling coefficients in the IPT–CPT integrated system, which is the guideline to balance the power contribution between the two couplings.

### B. Circuit Parameter Design

Using the integrated coupler in Table I, a 140-W input power inductive and capacitive integrated system is designed in this section. To simplify the design process, the circuit parameters are also designed to be symmetric from the primary to secondary side. According to (24) and the coupler parameters in Table I, the specifications and circuit parameters are calculated, which are given in Table II.

In the system, the input and output voltages are designed to be 50 V. The switching frequency is set to be 1 MHz to increase the CPT system power. The primary external inductance $L_{\text{ex1}}$ is 24.8 $\mu$H, and the secondary external inductance $L_{\text{ex2}}$ is slightly larger than $L_{\text{ex1}}$ to provide a soft-switching condition to the MOSFETs in the input inverter [21].

The system power can be regulated by adjusting $L_{\text{f}1}$ and $L_{\text{f}2}$, and they are both 1.54 $\mu$H to achieve 140-W system power. The equivalent inductive and capacitive coupling coefficient $k_{\text{I}}$ and $k_{\text{C}}$ are both 1.8%, Therefore, the two couplings contribute equally to the system power, which means $P_{\text{IPT}} = P_{\text{CPT}} =$ 70 W.

### C. System Simulation

Using the parameters in Table II, the system performance is simulated in LTspice. For simplicity, the power losses in the circuit components are also neglected. At 50 V input and output voltage condition, the simulation shows that the system achieves 140 W power. The simulated input and output voltage and current waveforms are shown in Fig. 7.

Fig. 7 shows that the voltage and current are almost in phase at both the input and output side. Also, the input voltage $V_1$ is about 90° lagging the output voltage $V_2$, which validates the circuit analysis in Section III. The input current $I_1$ is slightly lagging the input voltage $V_1$ to provide soft-switching condition to the MOSFETs.

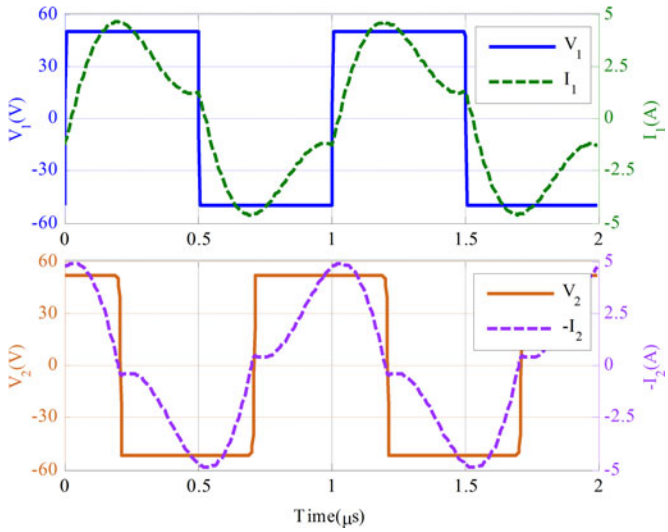


Fig. 7. LTspice-simulated input and output voltage and current waveforms.

TABLE III
RMS VALUE OF THE VOLTAGE STRESSON EACH COMPONENT

| Parameter | Voltage | Parameter | Voltage |
|---|---|---|---|
| $V_{\mathrm{Lf1}}$ | 35 V | $V_{\mathrm{Lf2}}$ | 35 V |
| $V_{\mathrm{Cf1}}$ | 55 V | $V_{\mathrm{Cf2}}$ | 55 V |
| $V_{\mathrm{Lex1}}$ | 720 V | $V_{\mathrm{Lex2}}$ | 720 V |
| $V_{\mathrm{P1-P2}}$ | 680 V | $V_{\mathrm{P3-P4}}$ | 680 V |
| $V_{\mathrm{P1-P3}}$ | 500 V | $V_{\mathrm{P2-P4}}$ | 560 V |

The circuit simulation by LTspice can also provide the voltage stress on each circuit component, as given in Table III. The voltages on $L_{\mathrm{f1}}$, $L_{\mathrm{f2}}$, $C_{\mathrm{f1}}$, and $C_{\mathrm{f2}}$ are relatively low, and the voltages across the external inductors $L_{\mathrm{ex1}}$ and $L_{\mathrm{ex2}}$ reach 720 V. In the integrated coupler, the voltages between the same-side strips $V_{\mathrm{P1--P2}}$ and $V_{\mathrm{P3--P4}}$ are both 680 V. The voltage between the transmitter and receiver strips $V_{\mathrm{P1--P3}}$ is 500 V, and $V_{\mathrm{P2--P4}}$ is 560 V. Since $d_1 = 1.2$ mm and $d = 18$ mm in this design and there are insulation taps between the adjacent strips, there is no concern about arcing between the strips.

The magnetic and electric field emissions of the coupler are also simulated in Maxwell to determine the safety-operation area. The voltages and currents acquired in circuit simulation are used as the excitations in the FEA simulation. The Maxwell simulation results are shown in Fig. 8.

Fig. 8(a) shows the magnetic field distribution around the integrated coupler. According to the circuit simulation, the current excitation flowing through each strip is about 4.6 A, and the transmitter and receiver currents are 90° out of phase. The direction of the currents is indicated in Fig. 5. Fig. 8(a) shows that the magnetic fields are concentrated in the center part of the coupler. The maximum magnetic field density between the transmitter and receiver is about 120 $\mu$T, and the safety limit of field density to human body is 27 $\mu$T at 1 MHz [26]. This shows that the magnetic field attenuates rapidly with distance, and the safe range is about 30 mm away from the coupler.

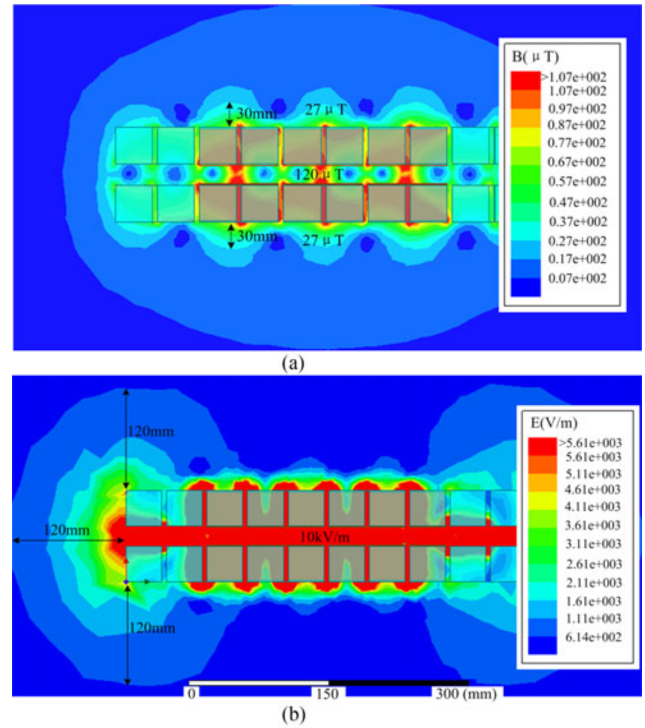


Fig. 8. Field emissions of the inductive and capacitive integrated coupler. (a) Magnetic field and (b) electric field.

Fig. 8(b) shows the electric field distribution around the integrated coupler. In the simulation, the voltages between the strips are the same with the values in Table III. Also, it shows that the electric fields are concentrated in the center part of the coupler. The maximum field strength in the center of the coupler is about 10 kV/m, and the safety limit of field strength is 614 V/m at 1 MHz [27]. The safe range is about 120 mm away from the coupler. Therefore, the electric field determines the safety working area of the coupler. In future research, the electric fields can be reduced by either reducing the voltage stress or using the electric field shielding method. Two large plates can be used in the coupler to reduce the electric field emissions without affecting the system power transfer capability [28].

## V. EXPERIMENTS

### A. Experimental Setup

Using the parameters in Table I, a prototype of the inductive and capacitive integrated coupler is constructed, as shown in Fig. 9. Multiple strips are screwed together to form the transmitter and receiver. Nylon spacers are used as the holder of the transmitter and receiver. The total size of the coupler is 468 mm × 468 mm. The parameter values of circuit components, including the integrated coupler, are measured by an Agilent E5072B network analyzer, as given in Table IV. The measured values are within ±10% tolerance of the desired values.

The experimental setup of the inductive and capacitive integrated system is shown in Fig. 10. The compensation circuit components values are the same with Table II. Since the skin

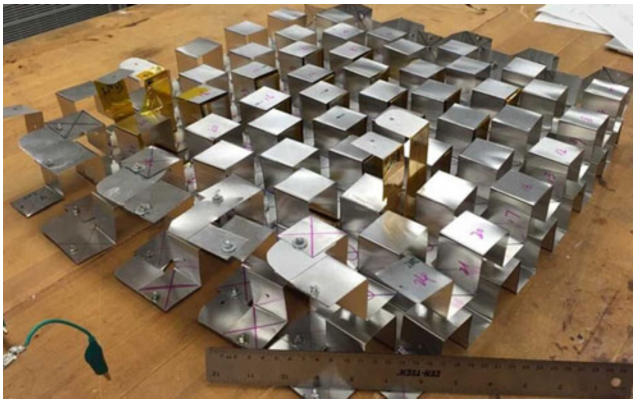

Fig. 9. Prototype of an inductive and capacitive integrated coupler.

TABLE IV
COMPARISON OF THE DESIGNED AND MEASURED PARAMETERS

| Parameter | Design Value | Measurement | Parameter | Design Value | Measurement |
|---|---|---|---|---|---|
| $L_{f1}$ | 1.54 $\mu$H | 1.45 $\mu$H | $C_{f1}$ | 16.5 nF | 16.4 nF |
| $L_{f2}$ | 1.54 $\mu$H | 1.42 $\mu$H | $C_{f2}$ | 16.5 nF | 16.4 nF |
| $L_1$ | 2.06 $\mu$H | 2.26 $\mu$H | $C_1$ | 910 pF | 942 pF |
| $L_2$ | 0.76 $\mu$H | 0.82 $\mu$H | $C_2$ | 910 pF | 931 pF |
| $L_3$ | 2.06 $\mu$H | 2.26 $\mu$H | $C_s$ | 16.7 pF | 18.1 pF |
| $L_4$ | 0.76 $\mu$H | 0.84 $\mu$H | $M_{eq}$ | 0.49 $\mu$H | 0.55 $\mu$H |
| $L_{ex1}$ | 24.8 $\mu$H | 24.6 $\mu$H | $L_{ex2}$ | 25.3 $\mu$H | 25.5 $\mu$H |

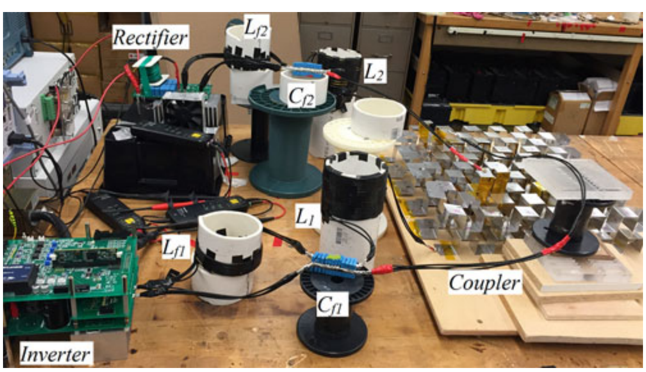


Fig. 10. Experimental setup of an inductive and capacitive integrated system.

depth of copper is 66 $\mu$m at 1 MHz, 2175-strand AWG 46 Litz wire with 40 $\mu$m diameter is used to make the compensation inductors $L_{f1}$, $L_{f2}$, $L_{ex1}$, and $L_{ex2}$. The compensation capacitors are high-power and high-frequency film capacitors from KEMET, and the dissipation factor is about 0.18% at 1 MHz. When connecting the coupler into the circuit, the polarity of the connection should follow Fig. 5 to maximize the system power.

Since the switching frequency is as high as 1 MHz, wide bandgap devices are used in this system. A general-purpose inverter consisting of silicon carbide (SiC) MOSFETs C2M0080120D is used at the input side to provide ac excitation. The digital controller TMS320F28335 is used to generate pulse-width modulation (PWM) signals for the MOSFETs, and the dead time between the PWM signals is about 60 ns to realize soft switching of the MOSFETs in the full-bridge inverter [25]. The output side rectifier uses SiC diodes IDW30G65C. In the future design, low-power devices will be used in the circuit to reduce the system cost and increase the efficiency.

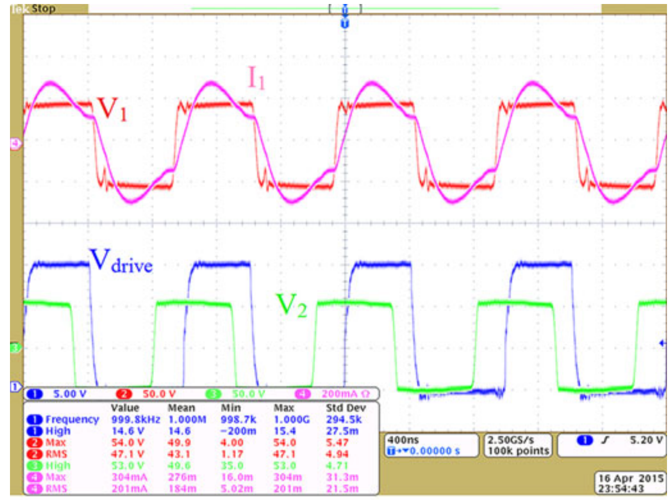


(a)

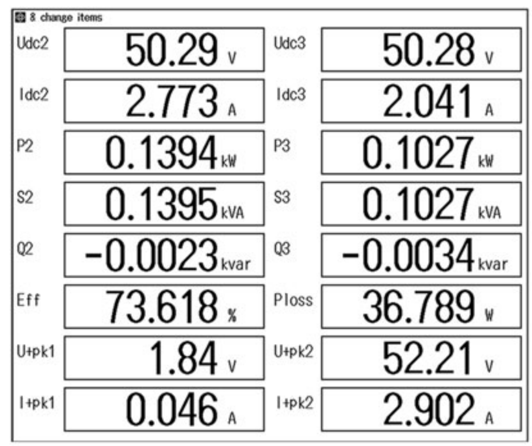


(b)

Fig. 11. Experimental results of inductive and capacitive integrated system. (a) Waveforms of voltages and currents. Ch 1 (blue): drive voltage $V_{\mathrm{drive}}$; Ch 2 (red): input voltage $V_1$; Ch 3 (green): output voltage $V_2$; Ch 4 (pink): input current $I_1$. (b) System power and efficiency.

### *B. Experimental Results*

Experiments are conducted using the setup in Fig. 10. A dc voltage source is used to supply power and an electronic dc load, working in constant voltage mode, is connected at the output side to emulate a battery load. When the input and output voltage are both 50 V, the experimental results are shown in Fig. 11.

Fig. 11(a) shows four channel measured waveforms. Channel 1 measures the driver signal of MOSFET, channel 2 measures the input voltage $V_1$, channel 3 measures the output voltage $V_2$, and channel 4 measures the input current $I_1$. Since a diode rectifier is used at the output, the output current $(-I_2)$ is in phase with the output voltage $V_2$, and its phase information is represented by $V_2$. In this high-frequency (1 MHz) system, the drive signal $V_{\mathrm{drive}}$ is very important because it relates to the switching performance of the MOSFET.

Fig. 11(a) shows that $V_1$ and $I_1$ are almost in phase with each other, which are consistent with the simulation waveforms in

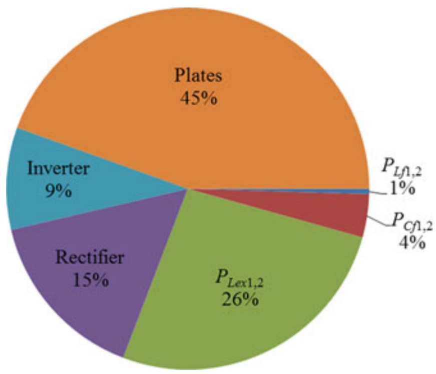


Fig. 12. Power loss distribution among the circuit components.

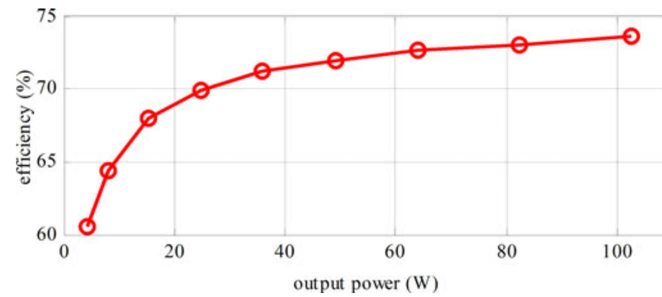


Fig. 13. Experimental dc–dc efficiency at different output powers.

Fig. 7. Therefore, the reactive power injected into the resonant circuit is limited and the unnecessary power losses are reduced. The waveform of input current $I_1$ is 10× scaled down by the probe in the measurement. The cutoff current at the switching transient is about 1 A and the soft-switching condition of the MOSFETs is achieved. At the output side, $V_2$ is about 90° leading the input voltage $V_1$, which also validates the circuit analysis in Section III. There is no noise in the driver signal $V_{\mathrm{drive}}$, so it is safe for long-time operation. The experimental waveforms in Fig. 11(a) are similar to those in Fig. 7. The slight differences in waveforms are caused by parameter differences between the actual system and the designed system, as given in Table IV.

Fig. 11(b) shows a screen shot from the power analyzer, indicating the system power and efficiency in the nominal input and output condition. The input power is 139.4 W, the output power is 102.7 W, the power loss is 36.7 W, and the efficiency from the dc source to dc load is 73.6%, including the MOSFETs and diodes. To confirm that the inductive and capacitive couplings in the integrated coupler both contribute to transferring power and their contributions are equal, the polarity of the coupler connection is flipped in further experiment, and the experimental result validates that there is no power received at the load side.

The experimental results in Fig. 11 show that the dc–dc efficiency of the designed IPT–CPT integrated system is relatively lower than a conventional IPT [11] or CPT system [21]. The power loss breakdown among the circuit components is estimated and shown in Fig. 12. The parasitic resistances of the MOSFETs, compensation inductors, and capacitors can be estimated from their datasheets and measurements [11]. The forward voltage of the diodes in the rectifier can also be obtained from the datasheet. Using the simulated currents flowing through the components, their power loss is therefore estimated. Since soft switching of MOSFET is realized, the switching loss can be neglected. The experimental total loss is 36.7 W in Fig. 11(b), and the remaining power losses should be in the integrated coupler.

Fig. 12 shows that the integrated coupler dissipates most of the power losses. It is because the qualify factor of the designed inductive and capacitive integrated coupler is relatively low. The coupler can generate both magnetic and electric fields, and the magnetic fields can induce extra eddy-current losses in the coupler, which lower the system efficiency. Considering the direction of the magnetic fields in the integrated coupler, its structure can be redesigned to reduce the eddy-current loss and improve its quality factor.

The other reason of low efficiency is that the inductive and capacitive coupling coefficients $k_{\mathrm{I}}$ and $k_{\mathrm{C}}$ in this system are only 1.8%, which is much lower than the conventional IPT or CPT systems. According to Li and Mi [29] and Lu *et al.* [30], the efficiency of an IPT or CPT system relates to the inductive and capacitive coupling coefficient and the components' quality factor. Lower coupling coefficient and quality factor result in lower system efficiency. In future design, $k_{\mathrm{I}}$ can be increased by increasing the coupler mutual inductance and decreasing the external inductance $L_{\mathrm{ex1}}$ and $L_{\mathrm{ex2}}$, and $k_{\mathrm{C}}$ can be increased by reducing the coupler self-capacitance $C_1$ and $C_2$.

The system dc–dc efficiency is also measured at different power level, which is shown in Fig. 13. The system efficiency increases with the increasing power. When the output power is higher than 30 W, the system can maintain a dc–dc efficiency higher than 70%.

### C. Discussion: Potential Benefits of an Integrated Coupler

Generally, an inductive and capacitive integrated coupler has three potential benefits compared to the conventional IPT or CPT system, which are addressed as follows.

First, the integrated coupler has the potential to increase the power density of a wireless power transfer (WPT) system. Since both magnetic and electric fields are used to transfer power, its power density can be higher than an IPT or CPT coupler.

Second, the integrated coupler has the potential to reduce the amount of compensation components. The self-inductance and self-capacitance of the integrated coupler can resonate together, which means the external circuit components can be reduced or even eliminated.

Third, the integrated coupler has the potential to reduce magnetic field emissions. The metal plates used in the coupler can work as shielding plates for the magnetic fields.

As a pioneering work studying an integrated coupler, the main contribution of this paper is to propose this integrated concept and validate its effectiveness. Since this is the very first attempt, the experimental results show that the proposed coupler in this paper has not realized the aforementioned three potential benefits of the integrated coupler.

Compared to the combined coupler in [23], the most important merit of this paper is that this is the first time to integrate inductive and capacitive couplers together into a single coupler. The demerit of this specific system is that the power density and efficiency is still lower than the combined coupler.

Considering the integrated design in this paper and the combined design in [23], there are a few possible directions to further improve the performance of an integrated coupler in future work. For example, the integrated coupler can utilizes spiral coils to increase its self-inductance and magnetic coupling coefficient. According to (25), the system power can therefore be increased and the power density can also be improved. Meanwhile, if the self-inductances of the coupler are large enough, the external inductances $L_{\rm ex1}$ and $L_{\rm ex2}$ can be eliminated to simplify the circuit topology. Moreover, Litz wire can be used to build the coupler to improve its quality factor. According to Li and Mi [29] and Lu *et al.* [30], if the coupling coefficient and quality factor are both increased, the system efficiency can therefore be significantly improvded. In this way, the efficiency of an integrated system can be comparable with the conventioanl IPT or CPT system. These will be investigated in future research, and the potential benefits of an integrated coupler could be realized.

## VI. Conclusion

This paper proposes an inductive and capacitive integrated coupler structure for wireless power transfer. Maxwell FEA simulation results of the coupler are provided, from which the equivalent circuit model is derived. An *LCL* compensated circuit topology is proposed to resonate with the coupler. The working principle and power expression are presented. A 140-W input power system is designed to demonstrate the proposed coupler structure. The main contribution of this paper is to propose a new concept to utilize both magnetic and electric fields in single coupler to realize wireless power transfer. In future research, the coupler structure and circuit parameters will be optimized to improve the system power and efficiency.

## References


[1] A. Abdolkhani, A. P. Hu, G. A. Covic, and M. Moridnejad, "Through-hole contactless slipring system based on rotating magnetic field for rotary applications," *IEEE Trans. Ind. Appl.*, vol. 50, no. 6, pp. 3466–3655, Nov./Dec. 2014.

[2] S. Aldhaher, P. C. Luk, A. Bati, J. F. Whidborne, "Wireless power transfer using class E inverter with saturable DC-feed inductor," *IEEE Trans. Ind. Appl.*, vol. 50, no. 4, pp. 2710–2718, Jul./Aug. 2014.

[3] M. Etemadrezaei and S. M. Lukic, "Multilayer tubular conductor for high Q-factor wireless power transfer system resonators," *IEEE Trans. Ind. Appl.*, vol. 52, no. 5, pp. 4170–4178, Sep./Oct. 2016.

[4] K. E. Koh, T. C. Beh, T. Imura, and Y. Hori, "Impedance matching and power division using impedance inverter for wireless power transfer via magnetic resonant coupling," *IEEE Trans. Ind. Appl.*, vol. 50, no. 3, pp. 2061–2070, May/Jun. 2014.

[5] J. Dai and D. Ludois, "A survey of wireless power transfer and a critical comparison of inductive and capacitive coupling for small gap applications," *IEEE Trans. Power Electron.*, vol. 30, no. 11, pp. 6017–6029, Nov. 2015.

[6] H. Zhang, F. Lu, H. Hofmann, and C. Mi, "A 4-plate compact capacitive coupler design and LCL-compensated topology for capacitive power transfer in electric vehicle charging applications," *IEEE Trans. Power Electron.*, vol. 31, no. 12, pp. 8541–8551, Dec. 2016.

[7] Y. Zhang, Z. Zhao, and K. Chen, "Frequency-splitting analysis of four-coil resonant wireless power transfer," *IEEE Trans. Ind. Appl.* vol. 50, no. 4, pp. 2436–2445, Jul./Aug. 2014.

[8] S. R. Cove and M. Ordonez, "Wireless-power-transfer planar spiral winding design applying track width ratio," *IEEE Trans. Ind. Appl.*, vol. 51, no. 3, pp. 2423–2433, May/Jun. 2015.

[9] C. Park, S. Lee, G. H. Cho, S. Y. Choi, and C. T. Rim, "Two-dimensional inductive power transfer system for mobile robots using evenly displaced multiple pickups," *IEEE Trans. Ind. Appl.*, vol. 50, no. 1, pp. 558–565, Jan./Feb. 2014.

[10] S. H. Lee, B. S. Lee, and J. H. Lee, "A new design methodology for a 300-kW, low flux density, large air gap, online wireless power transfer system," *IEEE Trans. Ind. Appl.*, vol. 52, no. 5, pp. 4234–4242, Sep./Oct. 2016.

[11] F. Lu, H. Zhang, H. Hofmann, and C. Mi, "A high efficiency 3.3 kW loosely-coupled wireless power transfer system without magnetic material," in *Proc. IEEE Energy Convers. Congr. Expo.*, 2015, pp. 2282–2286

[12] S. H. Lee and R. D. Lorenz, "Development and validation of model for 95%-efficiency 220-W wireless power transfer over a 30-cm air gap," *IEEE Trans. Ind. Appl.* vol. 47, no. 6, pp. 2495–2504, Nov./Dec. 2011.

[13] Z. Cheng, Y. Lei, K. Song, and C. Zhu, "Design and loss analysis of loosely coupled transformer for an underwater high-power inductive power transfer system," *IEEE Trans. Mag.*, vol. 51, no. 7, Jul. 2015, Art. no. 8401110.

[14] F. Lu, H. Hofmann, J. Deng, and C. Mi, "Output power and efficiency sensitivity to circuit parameter variations in double-sided LCC-compensated wireless power transfer system," in *Proc. IEEE Appl. Power Electron. Conf.*, 2015, pp. 507–601.

[15] J. Deng, F. Lu, S. Li, T. Nguyen, and C. Mi, "Development of a high efficiency primary side controlled 7kW wireless power charger," in *Proc. IEEE Int. Elect. Veh. Conf.*, 2014, pp. 1–6.

[16] L. Huang, A. P. Hu, A. Swain, and X. Dai, "Comparison of two high frequency converters for capacitive power transfer," in *Proc. IEEE Energy Convers. Congr. Expo.*, 2014, pp. 5437–5443.

[17] L. Huang, A. P. Hu, and A. Swain, "A resonant compensation method for improving the performance of capacitively coupled power transfer," in *Proc. IEEE Energy Conv. Congr. Expo.*, 2014, pp. 870–875.

[18] M. Kline, I. Izyumin, B. Boser, and S. Sanders, "Capacitive power transfer for contactless charging," in *Proc. IEEE Appl. Power Electron. Conf.*, 2011, pp. 1398–1404.

[19] D. C. Ludois, M. J. Erickson, and J. K. Reed, "Aerodynamic fluid bearings for translational and rotating capacitors in noncontact capacitive power transfer systems," *IEEE Trans. Ind. Appl.* vol. 50, no. 2, pp. 1025–1033, Mar./Apr. 2014.

[20] J. Dai and D. C. Ludois, "Capacitive power transfer through a conformal bumper for electric vehicle charging," *IEEE J. Emerg. Sel. Topics Power Electron.*, vol. 4, no. 3, pp. 1015–1025, Sep. 2016.

[21] F. Lu, H. Zhang, H. Hofmann, and C. Mi, "A double-sided LCLC-compensated capacitive power transfer system for electric vehicle charging," *IEEE Trans. Power Electron.*, vol. 30, no. 11, pp. 6011–6014, Nov. 2015.

[22] F. Lu, H. Zhang, H. Hofmann, and C. Mi, "A CLLC-compensated high power and large air-gap capacitive power transfer system for electric vehicle charging application," in *Proc. IEEE Appl. Power Electron. Conf.*, 2016, pp. 1721–1725.

[23] F. Lu, H. Zhang, H. Hofmann, and C. Mi, "An inductive and capacitive combined wireless power transfer system with LC-compensated topology," *IEEE Trans. Power Electron.*, vol. 31, no. 12, pp. 8471–8482, Dec. 2016.

[24] F. Lu, H. Zhang, H. Hofmann, W. Liu, and C. Mi, "An inductive and capacitive integrated coupler and its LCL compensation circuit design for wireless power transfer," in *Proc. IEEE Energy Convers. Congr. Expo.*, 2016, pp. 1–5.

[25] S. Li, W. Li, J. Deng, and C. C. Mi, "A double-sided LCC compensation network and its tuning method for wireless power transfer," *IEEE Trans. Veh. Techn.*, vol. 64, no. 6, pp. 2261–2273, Jun. 2015.

[26] International Commission on Non-Ionizing Radiation Protection, "guidelines for limiting exposure to time-varying electric, magnetic and electromagnetic fields (1 Hz to 100 kHz)," *Health Phys.*, vol. 99, pp. 818–836, 2010.

[27] *IEEE Standard for Safety Levels With Respect to Human Exposure to Radio Frequency Electromagnetic Fields, 3 kHz to 300 GHz*, IEEE Standard C95.1, 2005.

[28] H. Zhang, F. Lu, H. Hofmann, and C. Mi, "A six-plate capacitive coupler to reduce electric field emission in large air-gap capacitive power transfer," *IEEE Trans. Power Electron.,* to be published, doi: 10.1109/TPEL.2017.2662583.

[29] S. Li and C. Mi, "Wireless power transfer for electric vehicle applications," *IEEE J. Emerg. Sel. Topics Power Electron.*, vol. 3, no. 1, pp. 4–17, Mar. 2015.

[30] F. Lu, H. Zhang, H. Hofmann, and C. Mi, "An double-sided LC compensation circuit for loosely-coupled capacitive power transfer," *IEEE Trans. Power Electron.*, to be published, doi: 10.1109/TPEL.2017.2674688.

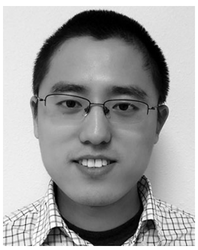

**Fei Lu** (S'12) received the B.S. and M.S. degrees in electrical engineering from the Harbin Institute of Technology, Harbin, China, in 2010 and 2012, respectively, and the Ph.D. degree in electrical engineering from the University of Michigan–Ann Arbor, Ann Arbor, MI, USA, in 2017.

He is currently a Postdoctoral Researcher with San Diego State University, San Diego, CA, USA. His research interests focus on wireless power transfer for the application of electric vehicle charging. He is working on the high-power and high-efficiency capacitive power transfer through an air-gap distance up to 100's of millimeters. He is also working on the application of wide bandgap devices on wireless power transfer system to increase the system frequency.

**Hua Zhang** (S'14) received the B.S. and M.S. degrees in electrical engineering from Northwestern Polytechnical University, Xi'an, China, in 2011 and 2014, respectively, and where she is currently working toward the Ph.D. degree in electrical engineering.

From September 2014 to August 2015, she was a joint Ph.D. student founded by the China Scholarship Council at the University of Michigan–Dearborn, Dearborn, MI, USA. Since September 2015, she has been with San Diego State University, San Diego, CA, USA. Her research interests focus on the coupler design of high-power inductive power transfer and capacitive power transfer system.

**Heath Hofmann** (M'89–SM'15) received the B.S. degree in electrical engineering from the University of Texas at Austin, Austin, TX, USA, in 1992, and the M.S. and Ph.D. degrees in electrical engineering and computer science from the University of California, Berkeley, CA, USA, in 1997 and 1998, respectively.

He is currently an Associate Professor with the University of Michigan–Ann Arbor, Ann Arbor, MI, USA. His research interests include the design, analysis, and control of electromechanical systems, and power electronics.

**Chunting Chris Mi** (S'00–A'01–M'01–SM'03–F'12) received the B.S.E.E. and M.S.E.E. degrees in electrical engineering from Northwestern Polytechnical University, Xi'an, China, in 1985 and 1988, respectively, and the Ph.D. degree in electrical engineering from the University of Toronto, Toronto, ON, Canada, in 2001.

He is currently a Professor and the Chair of electrical and computer engineering, and the Director of the Department of Energy-funded Graduate Automotive Technology Education Center for Electric Drive Transportation with San Diego State University (SDSU), San Diego, CA, USA. Prior to joining SDSU, he was at the University of Michigan–Dearborn, Dearborn, MI, USA, from 2001 to 2015. He was the President and the Chief Technical Officer of 1Power Solutions, Inc., Cupertino, CA, from 2008 to 2011. He is the Co-Founder of Gannon Motors and Controls LLC, San Diego, and Mia Motors, Inc., Dearborn. He has conducted extensive research, has published more than 100 journal papers, and delivered 30 invited talks and keynote speeches. He has taught tutorials and seminars on the subject of Hybrid Electric Vehicle (HEV) s/Plug-in Hybrid Electric Vehicle (PHEVs) for the Society of Automotive Engineers (SAE), the IEEE, workshops sponsored by the National Science Foundation, and the National Society of Professional Engineers. He has delivered courses to major automotive Original Equipment Manufacturer (OEMs) and suppliers, including GM, Ford, Chrysler, Honda, Hyundai, Tyco Electronics, A&D Technology, Johnson Controls, Quantum Technology, Delphi, and the European Ph.D. School. He has offered tutorials in many countries, including the U.S., China, Korea, Singapore, Italy, France, and Mexico. He has also served as a panelist at major IEEE and SAE conferences. His research interests include electric drives, power electronics, electric machines, renewable energy systems, and electrical and hybrid vehicles.

Dr. Mi received the Distinguished Teaching Award and the Distinguished Research Award from the University of Michigan–Dearborn. He also received the 2007 IEEE Region 4 Outstanding Engineer Award the IEEE Southeastern Michigan Section Outstanding Professional Award, and the SAE Environmental Excellence in Transportation (E2T) Award.